

XMM-Newton view of the shock heating in an early merging cluster, CIZA J1358.9–4750

Yuki OMIYA,^{1,*} Kazuhiro NAKAZAWA,^{1,10} Kyoko MATSUSHITA,² Shogo B. KOBAYASHI,² Nobuhiro OKABE,³ Kosuke SATO,⁴ Takayuki TAMURA,⁵ Yutaka FUJITA,⁶ Liyi GU,⁷ Tetsu KITAYAMA,⁸ Takuya AKAHORI,⁹ Kohei KURAHARA,⁹ and Tomohiro YAMAGUCHI¹

¹Departure of Physics, Nagoya University, Furo-cho, Chikusa-ku, Nagoya, Aichi 464-8601, Japan

²Department of Physics, Tokyo University of Science, 1-3 Kagurazaka, Shinjuku-ku, Tokyo 162-8601, Japan

³Department of Physics, Hiroshima University, 1-3-1 Kagamiyama, HigashiHiroshima, Hiroshima 739-8526, Japan

⁴Department of Physics, Saitama University, 255 Shimo-Okubo, Sakura-ku, Saitama 338-8570, Japan

⁵Institute of Space and Astronautical Science, Japan Aerospace Exploration Agency, 3-1-1 Yoshinodai, Chuo-ku, Sagami-hara, Kanagawa 229-8510, Japan

⁶Department of Physics, Graduate School of Science, Tokyo Metropolitan University, 1-1 Minami-Osawa, Hachioji-shi, Tokyo 192-0397, Japan

⁷SRON Netherlands Institute for Space Research, Utrecht, The Netherlands

⁸Department of Physics, Toho University, 2-2-1 Miyama, Funabashi, Chiba 274-8510, Japan

⁹Mizusawa VLBI Observatory, National Astronomical Observatory of Japan, 2-21-1, Osawa, Mitaka, Tokyo 181-8588, Japan

¹⁰Kobayashi-Maskawa Institute for the Origin of Particles and the Universe, Furo-cho, Chikusa-ku, Nagoya, Aichi 464-8601, Japan

*E-mail: omiya_y@u.phys.nagoya-u.ac.jp

Received (reception date); Accepted (acceptation date)

Abstract

CIZA J1358.9–4750 is a nearby galaxy cluster in the early phase of a major merger. The two-dimensional temperature map using XMM-Newton EPIC-PN observation confirms the existence of a high temperature region, which we call the “hot region”, in the “bridge region” connecting the two clusters. The ~ 500 kpc wide region between the southeast and northwest boundaries also has higher pseudo pressure compared to the unshocked regions, suggesting the existence of two shocks. The southern shock front is clearly visible in the X-ray surface brightness image and has already been reported by Kato et al. (2015). The northern one, on the other hand, is newly discovered. To evaluate their Mach number, we constructed a three-dimensional toy merger model with overlapping shocked and unshocked components in line of sight. The unshocked and preshock ICM conditions are estimated based on those outside the interacting bridge region assuming point symmetry. The hot region spectra are modeled with two-temperature thermal components, assuming that the shocked condition follows the Rankin-Hugoniot relation with the preshock condition. As a result, the shocked region is estimated to have a line-of-sight depth of ~ 1 Mpc with a Mach number of ~ 1.3 in the southeast

shock and ~ 1.7 in the northwest shock. The age of the shock waves is estimated to be ~ 260 Myr. This three dimensional merger model is consistent with the Sunyaev-Zel'dovich signal obtained using the Planck observation within the CMB fluctuations. The total flow of the kinetic energy of the ICM through the southeast shock was estimated to be $\sim 2.2 \times 10^{42}$ erg s^{-1} . Assuming that 10 % of this energy is converted into ICM turbulence, the line-of-sight velocity dispersion is calculated to be ~ 200 km s^{-1} , which is basically resolvable via coming high spectral resolution observations.

Key words: galaxies: clusters: individual (CIZA J1358.9-4750, RCX J1358.9-4750) — shock waves — turbulence — methods: data analysis

1 Introduction

Galaxy clusters are the largest self-gravitating system in the universe with a mass of $10^{14-15} M_{\odot}$, consisting of hundreds to thousands of galaxies. Nearly 80% of the mass is made up of dark matter, with member galaxies making up only $\sim 3\%$ (e.g., Vikhlinin et al. 2005; Sun et al. 2009; Sanderson et al. 2013; Akino et al. 2022). Most the hadronic matter is in the form of high temperature plasma, called an intracluster medium (ICM). Galaxy clusters are not isolated systems, but rather grow as they accumulate matter from their surroundings through gravitational interactions. One of the most common phenomena is a “major merger”, in which two galaxy clusters with close masses collide almost head-on. Depending on the mass of the cluster, a major merger can release up to 10^{64} erg of gravitational energy (e.g., Ricker 2004; Planelles & Quilis 2009; Mann & Ebeling 2012).

Numerical simulations have shown that a major merger event generates two types of shock waves (Miniati et al. 2000; Ryu et al. 2003; Skillman et al. 2008). When two clusters merge facing each other, the ICM in between is adiabatically compressed. As the collision velocity exceeds the ICM sound speed, two shock fronts are formed (e.g., Takizawa 2008; Akahori & Yoshikawa 2008; Akahori & Yoshikawa 2010; Ha et al. 2018). They move forward and backward along the merger axis, and eventually penetrate both systems, as seen in Abell 3667 (Nakazawa et al. 2009; Sarazin et al. 2010; Akamatsu et al. 2012a; Sarazin et al. 2016; de Gasperin et al. 2022), Abell 3376 (Bagchi et al. 2006; Kawano et al. 2009; Akamatsu et al. 2012b), and CIZA J2242.8+5301 (van Weeren et al. 2011; Okabe et al. 2015). Another shock wave, called the “equatorial shock wave”, appears perpendicular to the merger axis (e.g., Okabe et al. 2019), as observed in the merger of 1E 2216.0-0401 and 1E 2215.7-0404 (Gu et al. 2019). These shocks cause ICM heating, as well as ICM turbulence excitation, particle acceleration, and magnetic field amplification (e.g., Markevitch & Vikhlinin 2007; van Weeren et al. 2010). However, the branching energy ratio of these four phenomena is not well understood.

In order to estimate the energy input, it is necessary to construct the dynamical structures of merging clusters. Among

them, those in the early phase are relatively simple to model. In the early phase of a major merger, shock waves have not yet reached the outer edges of the cluster, and the outer regions mostly retain the pre-merger condition. Therefore, the properties of the “pre-merger” cluster can be well inferred. Once the initial conditions are known, it is relatively easy to elucidate the structure of the cluster in merging. When a shock wave is young, its Mach number is typically limited to less than 2 (Akahori & Yoshikawa 2010). In the late phase, it reaches ~ 4 (Ricker & Sarazin 2001).

CIZA J1358.9–4750 (hereafter, CIZA J1359) is a nearby galaxy cluster ($z=0.0074$; Piffaretti et al. 2011) listed in the Zone of Avoidance (CIZA) catalog (Ebeling et al. 2002, Kocevski et al. 2007). The X-ray centroid of the southeastern (SE) cluster is $14'$ (~ 1.2 Mpc) away from the northwestern (NW) cluster on the sky plane. The bridge region between the two is clearly visible in the X-ray image in figure 1.

Kato et al. (2015) observed CIZA J1359 with the Suzaku X-ray observatory and found a “brightness jump” in the southeast of the bridge region. This “brightness jump” was associated with a temperature jump, and the Mach number was calculated to be 1.32 ± 0.22 . Based on its typical “two clusters and a bridge” morphology and the presence of the narrow enhancement region, CIZA J1359 is claimed to be an early merger with its merger axis located approximately along the sky plane. Akahori et al. (2018) explored the existence of extended radio emission using the 16 cm band Australia Telescope Compact Array. Their main objective was to detect possible relic radio emissions, but they did not find any relic, halo, or mini-halo. Similarly, Kale et al. (2022) reported that there was no detection of diffuse cluster radio emission in the bridge region. The results suggest that CIZA J1359 is still in the early phase of the merger and that the shock front has not yet reached the outer edges of the cluster.

In this paper, we report the results of our analysis based on a deep XMM-*Newton* observation of this cluster. The outline of this paper is as follows. In Section 2, we describe the construction of a two-dimensional (2D) thermodynamic map and the discovery of the presence of two shock waves ~ 500 kpc apart.

In Section 3, we construct a three-dimensional (3D) model and discuss shocked conditions at two shock fronts. We assume $H_0 = 70 \text{ km s}^{-1} \text{ Mpc}^{-1}$, $\Omega_M = 0.3$ and $\Omega_\Lambda = 0.7$ (1 arcmin = 80.34 kpc at $z = 0.0074$) throughout this paper. Errors are given at the 68% confidence (1σ) level unless otherwise stated.

2 Data analysis

2.1 XMM-Newton observation

In this work, we used a 99 ks XMM-Newton observation on August 24–25, 2016, pointing to the center of the bridge region (obsid:0784980101). Among the European Photon Imaging Camera (EPIC) onboard XMM, EPIC-MOS1 CCD3 and CCD6, which cover the bridge region, were lost to the micrometeorite hit (Abbey et al. 2006; Snowden et al. 2008) and EPIC-MOS2 CCD4 and CCD5 are possibly in an anomalous state (e.g., Šuhada et al. 2012; Kuntz & Snowden 2008). The effective area of EPIC-PN is larger than that of the EPIC-MOS. In addition, there is a calibration inconsistency between EPIC-MOS and PN on the hardness of the spectra, especially in the higher energy band (e.g., Madsen et al. 2017). MOS tends to give a systematically harder photon index than PN and the Suzaku XIS detectors in this energy band. In ICM thermal fitting, the effect gives a much higher temperature than those obtained by Suzaku, especially when the ICM temperature is high (Kato et al. 2015, Kato 2018). To simplify this issue and because the EPIC-PN camera provides nearly two-thirds of the photon statistics in the bridge region of this observation, in this work, we focus on EPIC-PN data.

Standard processing of the observed data was performed using the Extended Source Analysis Software (ESAS), version 18.0.0, as described by Snowden et al. (2008), following the “cookbook for analysis procedures for XMM-Newton EPIC”¹. Calibrated photon event files were produced using the *epchain* task. We used the *pn-filter* task to remove proton contamination and produced a 65 ks Good Time Interval file. Figure 1 is a total counts image in 0.5–12 keV smoothed with $\sigma=2.5''$ Gaussian kernel created using the *pn-spectra* task.

2.2 2D thermodynamic mapping

To characterize the ICM in the bridge region, we generated thermodynamic maps. We first selected a circular region with a radius of $12'$ (~ 1 Mpc) centered on the bridge region, $(\alpha, \delta)_{J2000.0} = (13^{\text{h}}58^{\text{m}}39^{\text{s}}.3, -47^{\circ}46'29''.1)$, and divided it into about 180 regions, each containing approximately 2500 counts, based on the Weighted Voronoi Tessellations (WVT) binning algorithm (Diehl & Statler 2006). The spectra of each subregion were extracted and fitted with a thermal emission

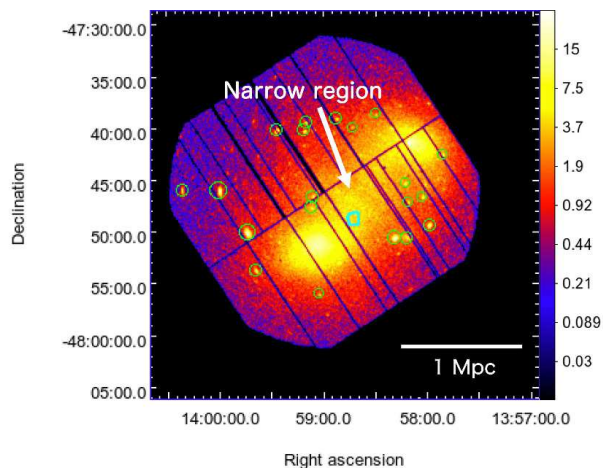


Fig. 1. A total counts X-ray image of CIZA J1359 observed with XMM-Newton EPIC-PN detector in 0.5–12 keV, smoothed with a Gaussian kernel with $\sigma = 2.5''$. The colorbar have the unit of counts. The green circles indicate the point source, which we removed in the analysis. The cyan polygon is the region from which the spectrum in figure 2 was extracted, corresponding to the SE3 in the upper right panel of figure 3.

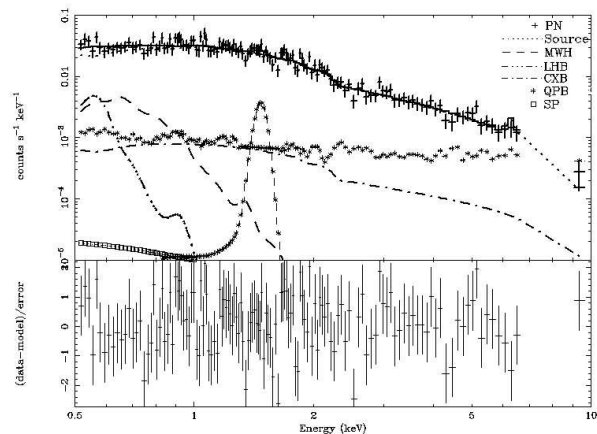


Fig. 2. The EPIC-PN spectra with the QPB component subtracted in the polygon region indicated by cyan in figure 1. The solid line represents the overall best-fit model. Its individual modeled components (source and backgrounds) are shown in the legend.

model, using *xspec* v12.12.0 (Arnaud 1996).

As an example of spectral fitting, figure 2 shows the results in the region indicated by cyan in figure 1. Quiescent particle background (QPB) spectra were generated by the *pn-back* task and subtracted from the source spectra. The Al $K\alpha$ emission line was modeled as a Gaussian, and the 7–9 keV band was ignored in the fitting to avoid other instrumental background lines. As a sky background, three components were modeled; Local Hot Bubble (LHB) radiation with a temperature fixed at 0.1 keV, Milky Way Halo (MWH) radiation with a temperature fixed at 0.23 keV, and Cosmic X-ray Background (CXB). The LHB and MWH were modeled using *apec* models with a metal abundance fixed at the solar value (Anders & Grevesse 1989), and their normalizations were determined by

¹ <http://heasarc.gsfc.nasa.gov/docs/xmm/esas/cookbook>

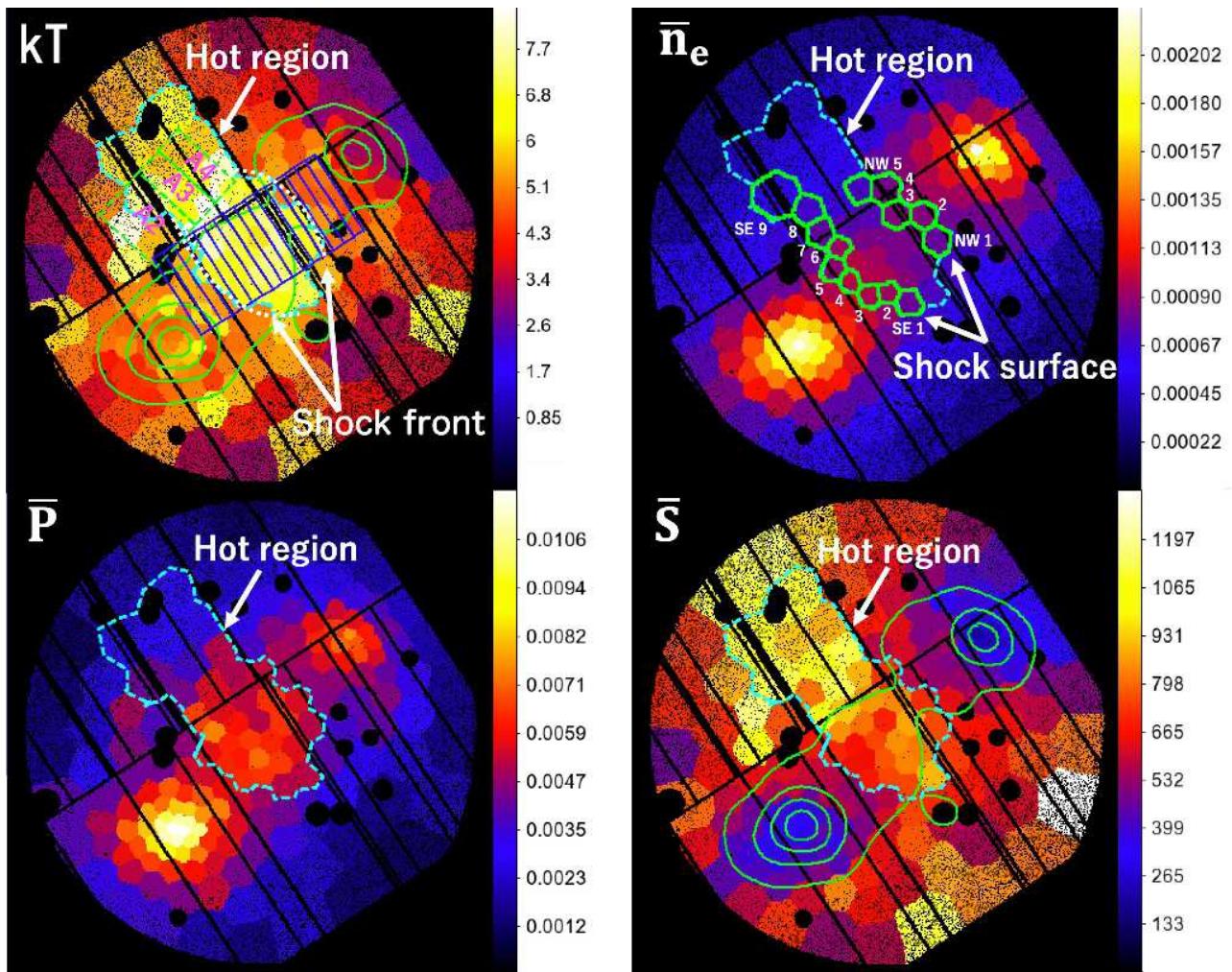


Fig. 3. Thermodynamic maps with regions divided by the WVT binning algorithm. The upper-left panel shows a temperature map overlaid with green contours for X-ray surface brightness. The cyan dotted line shows the hot region we define, and the blue boxes are the projection regions discussed in Section 2.3. Green-dotted boxes indicate the regions of A2, A3, and A4 given in Kato et al. (2015), respectively. The pseudo-density (upper right), pseudo-pressure (lower left), and pseudo-entropy (lower right) maps assume that the ICM is uniformly spread over the line-of-sight depth of 1 Mpc. Units of 2D temperature, pseudo-density, pseudo-pressure, and pseudo-entropy maps are keV, $\text{cm}^{-3} \times (l/1 \text{ Mpc})^{-1/2}$, $\text{keV cm}^{-3} \times (l/1 \text{ Mpc})^{-1/2}$ and $\text{keV cm}^2 \times (l/1 \text{ Mpc})^{1/3}$, respectively.

fitting the outermost region of the data after discarding sources that have fluxes of more than $1.0 \times 10^{-14} \text{ erg s}^{-1} \text{ cm}^{-2}$ in 0.4–7.2 keV using the ESAS *cheese* task, indicated by green circles in figure 1. The CXB spectrum is modeled with a power law of the photon index of -1.41 . Its normalization is fixed at $5.7 \times 10^{-8} \text{ erg s}^{-1} \text{ cm}^{-2} \text{ st}^{-1}$ at 2–10 keV (Nakazawa et al. 2009) because five Suzaku mapping observations showed that the ICM component filled the entire XMM field of view (Kato 2018), and the CXB normalization cannot be estimated from the XMM data. Strictly speaking, CXB normalization from Nakazawa et al. (2009) is obtained by removing sources with flux exceeding $2.0 \times 10^{-14} \text{ erg s}^{-1} \text{ cm}^{-2}$, which differs from our case. However, as figure 1 shows, the ICM contamination make it difficult to remove all sources with the value. Also, even if we change the CXB normalization by 20%, our

results did not change within 0.3% around the bridge, and 3% at the outermost regions. Therefore, we continue using $5.7 \times 10^{-8} \text{ erg s}^{-1} \text{ cm}^{-2} \text{ st}^{-1}$ at 2–10 keV as the CXB normalization, for simplicity. A residual soft-proton (SP) contamination that is not filtered by the *pn filter*, was incorporated as a broken power law model with a cutoff of 3.0 keV (Kuntz & Snowden 2008).

To reproduce the source radiation, we used a collisionally ionized diffuse thermal plasma model absorbed by the galactic absorption (*phabs* × *apec*). The redshift was fixed at 0.07 (Kato et al. 2015). The metal abundance was fixed at 0.3 solar following Fukazawa et al. (2004) and Ghizzardi et al. (2021) who used Anders & Grevesse (1989) abundance table. As a note, performing a spectral fit with Lodders et al. (2009) abundance table as a trial does not significantly ($\sim 1\%$) change the param-

eters of the source radiation. The hydrogen column density was fixed at $1.15 \times 10^{21} \text{ cm}^{-2}$, determined from the HI map by the Leiden / Argentina / Bonn (LAB) survey (Kalberla et al. 2005). The chi-squared statistic was used to evaluate the goodness of fit. By fitting the spectra of each sub-region, we obtained a two-dimensional temperature ($2D \ kT$) map (the upper left panel of figure 3).

The $2D \ kT$ map shows the existence of a high temperature region in the bridge region. We define this 6–8 keV high-temperature region, enclosed by the cyan dotted line in the map, as the “hot region”. It extends 500 kpc along the merger axis. On the SE side boundary of the hot region, the temperature increases from ~ 5 keV to ~ 7 keV. This jump is associated with a narrow enhanced emissivity (see figure 1). Compared to the Suzaku results described by Kato et al. (2015), the location of the temperature jump between their A2, A3 and A4 regions is consistent with that jump shown in our $2D \ kT$ map obtained from the XMM EPIC-PN data. The temperature values themselves are statistically consistent, as well (see figure 3 in Kato et al. 2015). Furthermore, a similar temperature jump is observed at the NW edge of the hot region, from ~ 4 keV to ~ 7 keV. This was not well resolved in the first Suzaku observation (Kato et al. 2015), probably due to its moderate angular resolution. On the basis of their geometry, we considered these two edges as candidates for forward and backward shock waves.

To better confirm these shocks, we created the $2D$ pseudo electron density (\bar{n}_e), pressure (\bar{P}), and “astrophysical entropy” (\bar{S}) maps, also shown in figure 3. The \bar{n}_e was obtained from the normalization of the *apec* model by assuming that the ICM is uniformly spread over the line-of-sight depth of 1 Mpc and that the electron density \bar{n}_e and hydrogen density \bar{n}_H satisfy the relation $\bar{n}_e = 1.2\bar{n}_H$ considering the full ionization of helium. The \bar{P} and \bar{S} were calculated as $\bar{P} = \bar{n}_e kT$ and $\bar{S} = \bar{n}_e^{-2/3} kT$, respectively. The $2D \ \bar{P}$ map shows a clear enhancement at the SE edge. A similar enhancement is also marginally suggested at the NW edge.

2.3 Estimating the ICM parameters around the two shock candidates

To investigate jump conditions, we created $1D$ thermodynamic profiles along the hot region. For this purpose, the regionalization using the WVT algorithm is not appropriate because it is non-biased, based only on photon statistics, and not optimized to obtain ICM parameter differences perpendicular to the possible SE shock front observed in the X-ray image. We selected a rectangular region in the bridge as shown in the upper left panel of figure 3. The region is then divided into 16 subregions, each with $36''.5 \times 280''$ area. The $1D$ temperature profile thus obtained is shown in figure 4a. A pair of jumps in temperature are clearly visible. Similarly, \bar{P} and \bar{S} clearly show a pair of jumps

in the same location (see figures 4c and 4d). The increase in pressure and entropy suggests that the two temperature jumps in the SE and NW are due to shock and not adiabatic compression.

From these temperature jumps, the Mach numbers were estimated to be $M_{SE} = 1.25^{+0.15}_{-0.13}$ for the SE shock and $M_{NW} = 1.28^{+0.19}_{-0.17}$ for the NW shock using the following Rankine–Hugoniot equation (R–H),

$$\frac{kT_2}{kT_1} = \frac{5M^4 + 14M^2 - 3}{16M^2}. \quad (1)$$

Here, the subscripts 1 and 2 denote pre-shock and shocked conditions, respectively. In this $1D$ analysis, we chose “pre-shock” and “shocked” regions as the ones closest to the shocks. The Mach number for the SE shock is consistent within error with 1.32 ± 0.22 , the value obtained from the Suzaku observation (Kato et al. 2015).

On the contrary, no positive jumps in \bar{n}_e are observed at the candidate shock wave locations, as shown in figure 4b. However, the ICM density of each cluster rapidly decreases with distance from the center, and a possible positive density jump could be smeared by its gradient. Therefore, the density distribution had better be compared to the pre-shock condition value. To address this possibility, we constructed $3D$ ICM profiles based on a few simple assumptions in the next section.

Focusing within the hot region, the \bar{n}_e profile shows a two bins wide (~ 100 kpc) dip region in the center. It is decreased by about 10% compared to the neighboring regions, respectively. The feature could be caused by local shortage of depth of ICM emission, but more likely simply reflecting the density decrease. Such a low surface brightness structure is called a channel, and a similar feature has been reported in some clusters, such as Abell 85 (Ichinohe et al. 2015). Across the left boundary of the channel, the temperature has not changed within statistical error, but across the right side, it has increased by about 1 keV. Thus, the \bar{P} profile shows a decrease in the left side and resumes in the right side. Similarly, the \bar{S} profile shows almost no change in the left side and an increase by about 20% in the right side. In short, the channel region has either lower ICM pressure or higher entropy. These features of channel would be caused by “non-thermal pressure” of magnetic or cosmic-ray origins or “turbulence pressure”. It is also possible that it is affected by the high entropy ICM of the outer edge of the pre-collision cluster because this channel region is located roughly at the middle of the two clusters, and the contact surface (if not strongly mixed yet) of the two clusters will reside here. Although this is clearly an interesting signature, a lack of data statistics prevents us from further analysis. In the $3D$ modeling presented later, to avoid the central regions, we will just focus on the thermal parameters at the edge of the hot region around the shock plane.

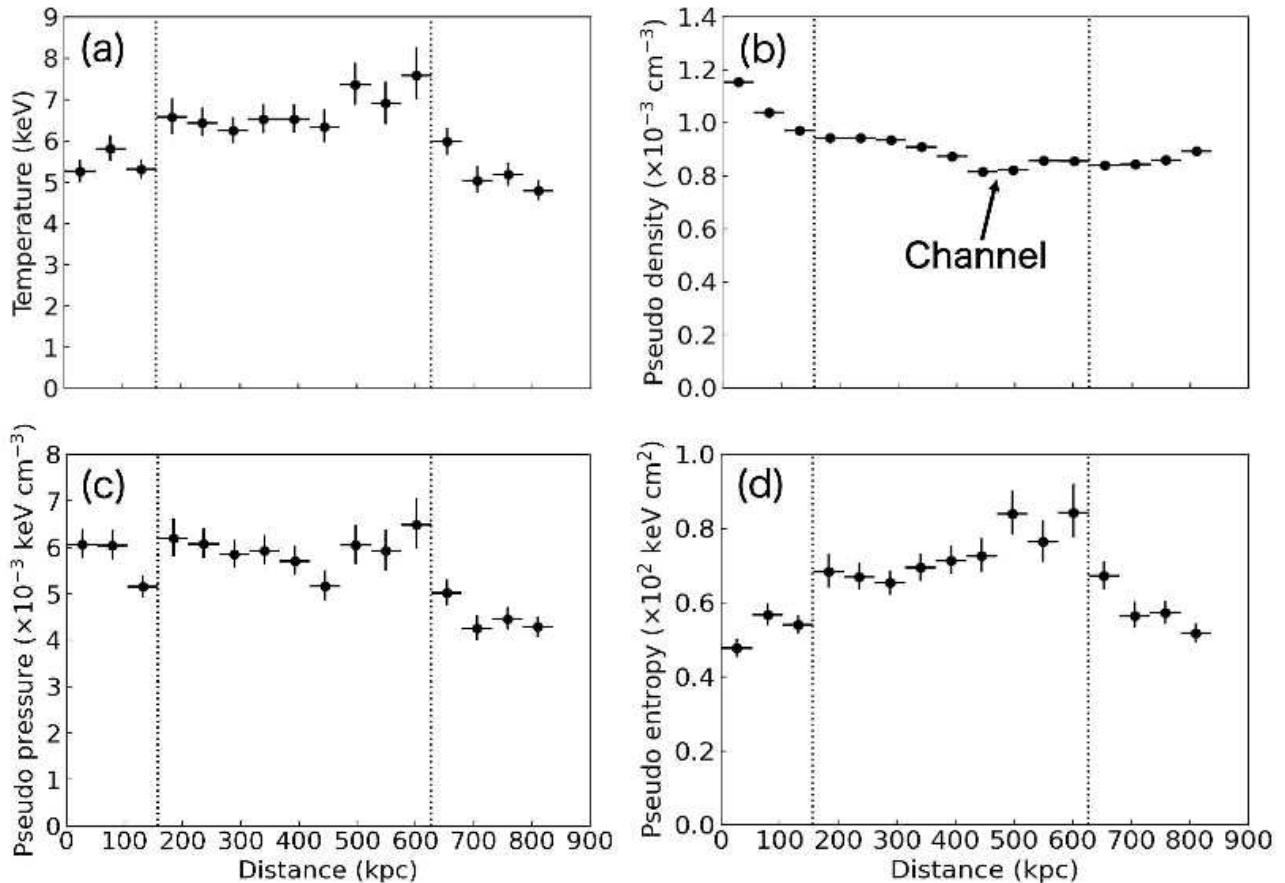


Fig. 4. 1D temperature (a), pseudo density (b), pseudo pressure (c), and pseudo entropy (d) profiles from SE to NW. We divided 16 blue regions of $37''.5 \times 280''$ strips, as shown in the upper left panel of figure 3. The vertical dotted-lines indicate the shock fronts at SE (left side) and NW (right side), respectively.

3 Simple 3D modeling of the merger

3.1 The 3D original cluster model in the unshocked region

The 2D kT map and 1D profile strongly suggest that there are two shock waves in the bridge region. This in turn means that the ICM in the “outside regions” is unaffected by the shocks, and record their pre-merger conditions. In addition, the two clusters are located about 70% of the r_{200} of each other. Here, the r_{200} estimated from the temperature at the center of the cluster is 1.8 Mpc in the NW and 2.1 Mpc in the SE cluster, respectively (Kato 2018). As such, ICM in the outside regions is not expected to be greatly affected by tidal forces. Here, for simplicity, we assumed that the two clusters are individually point-symmetric, and thus the ICM properties in the “inside region” before the collision can be estimated using a model parameterizing those in the outside regions. We modeled them three-dimensionally and hence call it a “3D original cluster model”.

To construct a temperature distribution of the 3D original cluster model, we selected $7''.5$ semicircular regions within the outside regions, indicated by green in the right panel of figure 5. These semicircular regions were divided into annular

sub-regions with radii of $0''-1'', 1''-1.5'', 1.5''-2'', 2.5''-3'', \dots, 6.5''-7'', 7''-7.5''$ from each cluster center. The spectra of individual small regions were fitted to obtain the two-dimensional temperature radius distribution for the NW and SE clusters, respectively, as shown in figure 5.

Next, the spectra were de-projected using the *xspec*’s *project* function to obtain the best-fit 3D temperature profiles. The outer two bins were excluded in the temperature distribution because they are considered to be deeply affected by the overly simplistic boundary condition of ignoring radii above $7''.5$ (e.g., Johnstone et al. 2005; Russell et al. 2008). The 3D original cluster temperature model was then parameterized based on the following formula given by Vikhlinin et al. (2006),

$$T(r) = t_0 \frac{(r/r_t)^{-a}}{[1 + (r/r_t)^b]^{c/b}}. \quad (2)$$

The best-fitting parameters for each cluster are listed in table 1.

Following kT distribution, a 3D ICM density distribution in the unshocked region was created. We created 0.5–10 keV energy band image excluding the Al-line band (1.3–1.9 keV). The entire bridge region, indicated by a green box in the right panel of figure 6, point sources, and CCD dead spaces were

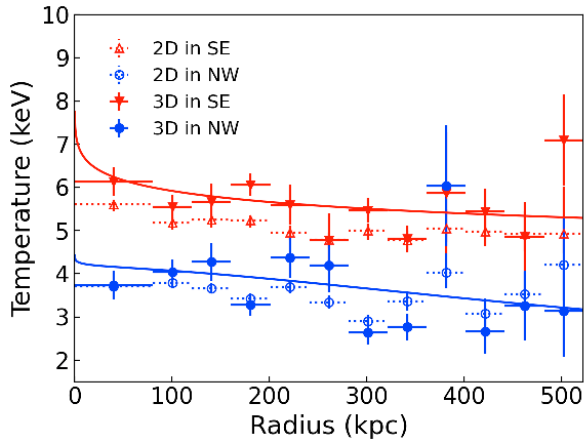


Fig. 5. The temperature distributions of the 3D original cluster model in the NW and SE clusters, respectively. Solid lines show the results of the fitting of the 3D temperature distributions in the NW and SE cluster with the 3D temperature model function given in Vikhlinin et al. 2006, respectively.

Table 1. Parameters of 3D temperature original cluster model

Region	t_0 (keV)	r_t (kpc)	a	b	c
NW	4.07 ± 0.30	85	0.01	0.3	0.1
SE	7.56 ± 0.50	425	0.01	2.0	0.5

also excluded. The QPB component was subtracted from the created image, and an exposure correction was applied to that image. We executed simultaneous fitting on the created images with two β model distributions of elliptical surface brightness and constant background component models for the NW and SE clusters (β model_{NW} + β model_{SE} + const). For simplicity, the β models obtained from the surface brightness fitting were transformed into β density models assuming that the shape of the galaxy clusters was an oblate ellipsoid to obtain a 3D ICM density distribution. The equation is given by the following formulas:

$$n(r) = n_0(1 + (r/r_c)^2)^{-3\beta/2}, \quad (3)$$

$$r = [x'^2 + (y'/\epsilon)^2]^{1/2}, \quad (4)$$

$$x' = (x - x_0) \cos \theta + (y - y_0) \sin \theta, \quad (5)$$

$$y' = (y - y_0) \cos \theta - (x - x_0) \sin \theta, \quad (6)$$

where x_0 and y_0 are the coordinates of the center of the galaxy cluster, ϵ is the ellipticity (the ratio of the minor axis to the major axis), and θ is the angle of the major axis measured counter-clockwise from the west direction.

Table 2. Parameters of 3D density original cluster model

Region	n_0 10^{-3} cm^{-3}	r_c (kpc)	β	ϵ	θ (degree)
NW	2.54 ± 0.19	165	0.67	0.68	348
SE	3.09 ± 0.11	188	0.53	0.66	26

The fitted model image is shown in the left panel of figure

6 and individual best fitting parameters are shown in table 2. The right panel of figure 6 shows a ratio map of observed and modeled images applied to the WVT binning algorithm to evaluate the residual of the surface brightness fitting. This ratio image shows that in the outer regions the model and observations mostly agree, while in the bridge region there is an increase in the ratio of more than 20%. The spread of the ratios in the outer regions was $\pm 15\%$ for the NW and $\pm 7.5\%$ for the SE clusters, respectively. As the density fluctuation of the 3D original cluster model, the square root of these spreads was handled when evaluating the uncertainties of the parameters in the following analyses.

Similarly, we created the 2D emission-weighted temperature map by combining the 3D original cluster temperature and density models. Our temperature model reproduces the observed 2D kT map very well, except for the inside (or bridge) region. Figure 7 shows a ratio map of the 2D kT map and the 2D emission-weighted temperature map using the 3D original cluster model, with the WVT binning. In the outside region, the deviations between model and observation were estimated to be 7.4% for the NW and 6.4% for the SE clusters, respectively. These uncertainties were included as the fluctuation of the 3D original cluster temperature model.

Overall, the enhanced region in the 2D kT ratio map coincides well with the ‘‘hot region’’ on the 2D kT map (the top left panel of figure 3), as well as the enhanced region in the surface brightness ratio map. Actually, the spread of the surface brightness enhancement is more robust and smooth than the rather noisy enhancement in the 2D kT map.

3.2 The 3D merger model around the bridge region

We successfully extracted the shock-wave enhancement region by restoring the 3D original cluster distribution. In other words, the apparent lack of density increase at the shock front in the 1D density profile (the upper right panel of figure 4) can be well explained as caused by the original ICM density gradient before merging. Then, are the enhancement values of the temperature and X-ray surface brightness at the shock surface consistent? We estimate the Mach numbers from the temperature and density ratio at the shock surface, respectively, using the R-H equation expressed in equation (1) and the following equation,

$$\frac{n_2}{n_1} = \frac{4M^2}{M^2 + 3}, \quad (7)$$

where the subscripts 1 and 2 indicate pre-shock and shocked conditions, respectively. For simplicity, the density ratio is calculated as the square root of the X-ray surface brightness ratio. We defined the shock front candidate regions as SE 1–9 and NW 1–5, located at the edge of the hot region, as shown in the upper right panel of figure 3. Figure 8 shows the Mach numbers estimated from the temperature and density ratios for

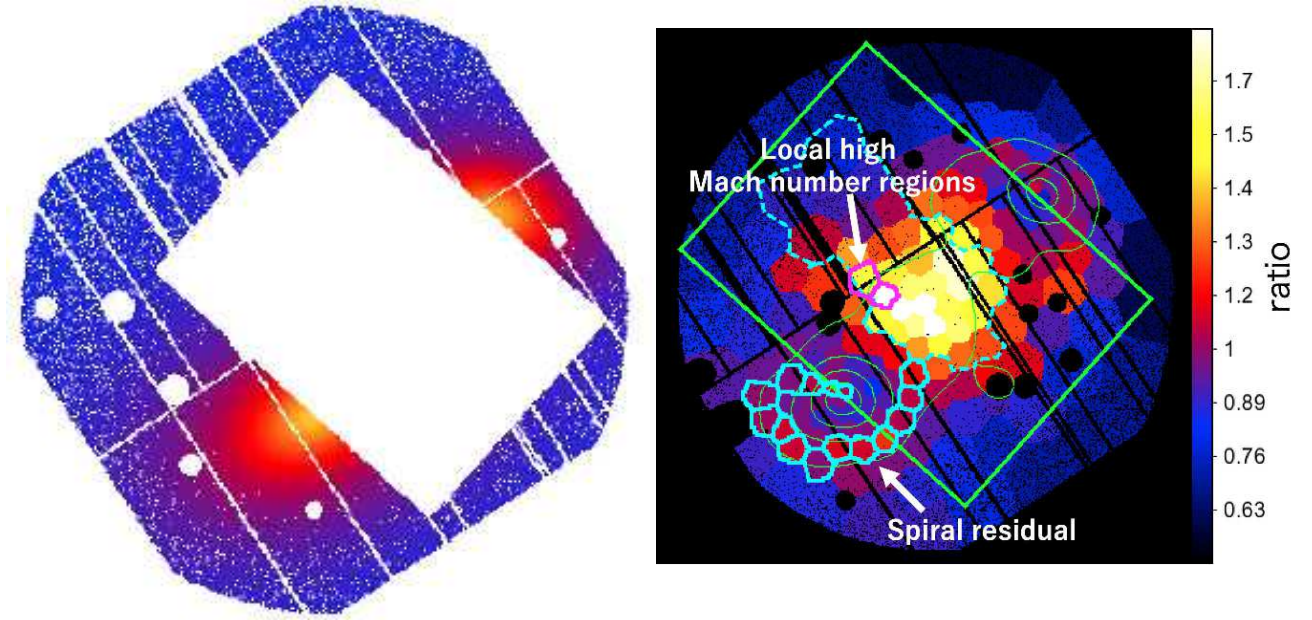


Fig. 6. Left: An image of the X-ray surface brightness model estimated from the two β models. Areas excluded in the fitting process, such as the bridge region, are removed. The best-fitting parameters are listed in table 3. Right: X-ray surface brightness ratio map of the model and observed images binned by the WVT algorithm. The green box indicates the areas excluded for the construction of the 3D original cluster density model. Cyan polygon regions are those with the spiral positive residual structure described in Section 3.5. The magenta polygon regions are the local regions with higher Mach numbers than the other regions indicated by the 3D merger model (see figure 10), corresponding to SE 6 and 7.

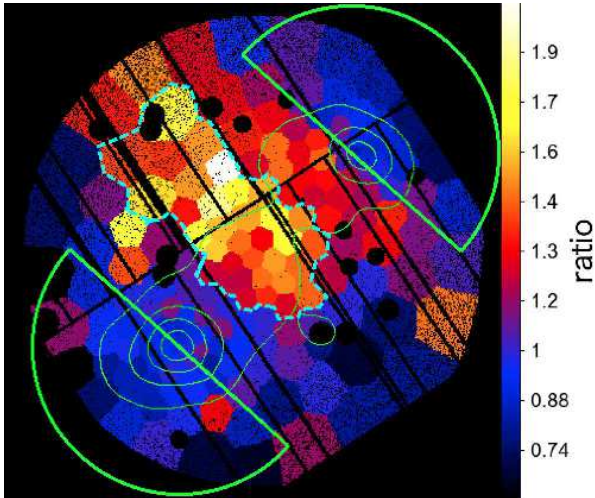


Fig. 7. A ratio map of the $2 kT$ map and the emission-weighted temperature map based on the 3D original cluster model. The green semicircular region indicates the non-shocked region selected for the construction of the 3D original cluster model. The dotted cyan line indicates the hot region.

individual regions. Overall, the Mach numbers for the temperature are clearly larger than the Mach numbers for the density. Because the Mach numbers obtained from temperature and density jumps are inconsistent, it is likely that the shocked and unshocked components overlap on the line of sight within the hot region. Therefore, we tried to fit the spectra with a two-temperature ($2 kT$) model to derive the thicknesses in the line

of sight of the shocked and unshocked components, l_s and l_{us} , respectively. However, as discussed in the Appendix, neither the shocked temperature (kT_s) nor the l_s can be determined simply by fitting the $2 kT$ model with both parameters set free.

Here we introduced another simple assumption that the shocked and unshocked components have the 3D-special structure shown in figure 9. The ICM parameters for the unshocked component can be estimated from the 3D original cluster model. The preshock condition, which is the state in the shocked region if the shock wave did not pass through, can also be estimated using the same model, and the R-H relations shown in equations (1) and (7) are assumed between the shocked and preshock components on the shock wave surface. Precisely speaking, this assumption is valid only at the edge region of the shock because the post-shock region is already compressed, and thus its pre-shock condition is difficult to estimate. We therefore focus on the shock front candidate regions for a moment. As a reminder, we note here that the subscripts “s”, “un”, and “pre” labels mean those for the shocked condition, unshocked condition, and preshock condition of the shocked region, respectively. The derivation of the l_s and Mach numbers proceeded specifically as follows.

1. Assuming l_s , the $norm_{us}$ and kT_{us} of the unshocked component can be calculated from l_{us} and the 3D original cluster model by emission weighting (here ICM was considered up to r_{200}).

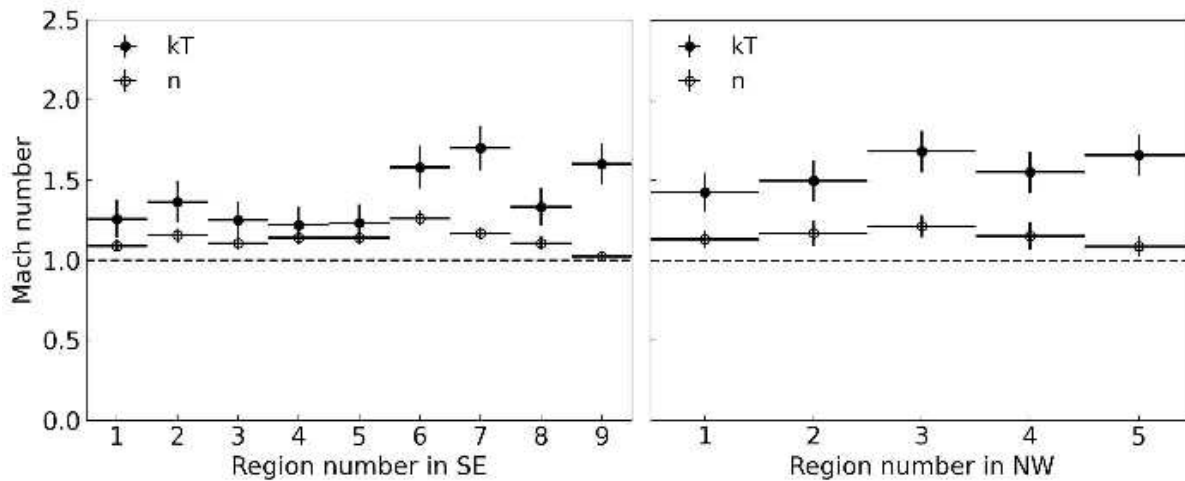


Fig. 8. The Mach number distributions derived from the temperature (kT) and density (n) ratios at the SE (left) and NW (right) shock fronts. For simplicity, the density ratio is calculated as the square root of the surface brightness ratio.

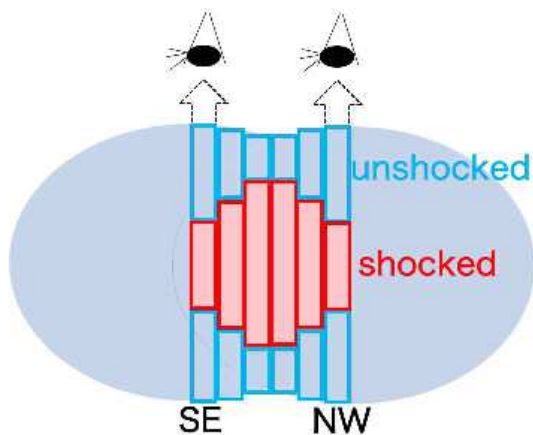


Fig. 9. The concept of 3D merger modeling. The shocked and unshocked regions are indicated by red and blue, respectively.

2. With the low temperature component, kT_{US} and $norm_{\text{US}}$, fixed at this calculated value, a spectral fit of the two temperature model was performed to derive $norm_{\text{S}}$ and kT_{S} for the high temperature component.
3. Similarly, n_{pre} and kT_{pre} for the preshock condition can be calculated from the 3D original cluster model by weighting. Then, by applying the R-H relation for the density and the temperature, two estimations of Mach number can be calculated.
4. After repeating this calculation for various l_{s} , the depth l_{s} was derived by finding the point where the two Mach numbers are consistent.

Details are given in the Appendix.

The results are summarized in figure 10. The Mach numbers are about ~ 1.3 for the SE shock surface (excluding the region number 6–7) and ~ 1.7 for the NW shock surface. In both cases, kT_{S} is ~ 8 keV, n_{S} is $\sim 1.0 \times 10^{-3} \text{ cm}^{-3}$ and l_{s} is ~ 1 Mpc.

3.3 Comparison with Planck SZ signal

In this section, we verified the 3D merger model with the Sunyaev-Zel'dovich (SZ) effect signal using the Planck satellite observations. The 3D merger model showed that the shock planes have a post-shock region sandwiched between two shocks with Mach numbers ~ 1.7 in NW and ~ 1.3 in SE, with a depth of ~ 1 Mpc.

The combination of X-ray surface brightness and the Compton y -parameter gives us information about depth and electron density because of their different dependence on electron temperature and density (e.g., Akamatsu et al. 2017; Hincks et al. 2022). We use the y map obtained using the Planck Release2 Needlet Independent Linear Combination (NILC; Delabrouille et al. 2009; Remazeilles et al. 2013) method. Figure 11a shows the y map provided by the Planck collaboration (Planck Collaboration et al. 2016) of the $123' \times 123'$ square region centered on CIZA J1359, $(\alpha, \delta)_{J2000.0} = (13^{\text{h}}58^{\text{m}}30^{\text{s}}.0, -47^{\circ}45'00''.0)$. We note here that the y map produced by NILC is convolved with a Gaussian kernel with $\text{FWHM}=10'$, and therefore it is impossible to directly compare it with our X-ray maps. In the $41' \times 41'$ square region of figure 11a indicated by the magenta dotted line, we calculated the y -parameter based on the 3D merger model and convolved it with the same FWHM as shown in figure 11b. For simplicity, the post-shock ICM condition is assumed to be constant from the shock front to the contact surface (at the middle of the channel. See section 2.3) and spread over a depth of 1 Mpc. Although being too much simplified, the density and temperature distribution shown in figure 4 is largely consistent with this assumption. To check the consistency of the model with the observed data, we created the residual map by subtracting the calculated map from the observed map as shown in figure 11c. The residual difference is about 3.0×10^{-6} , which is consistent with the CMB

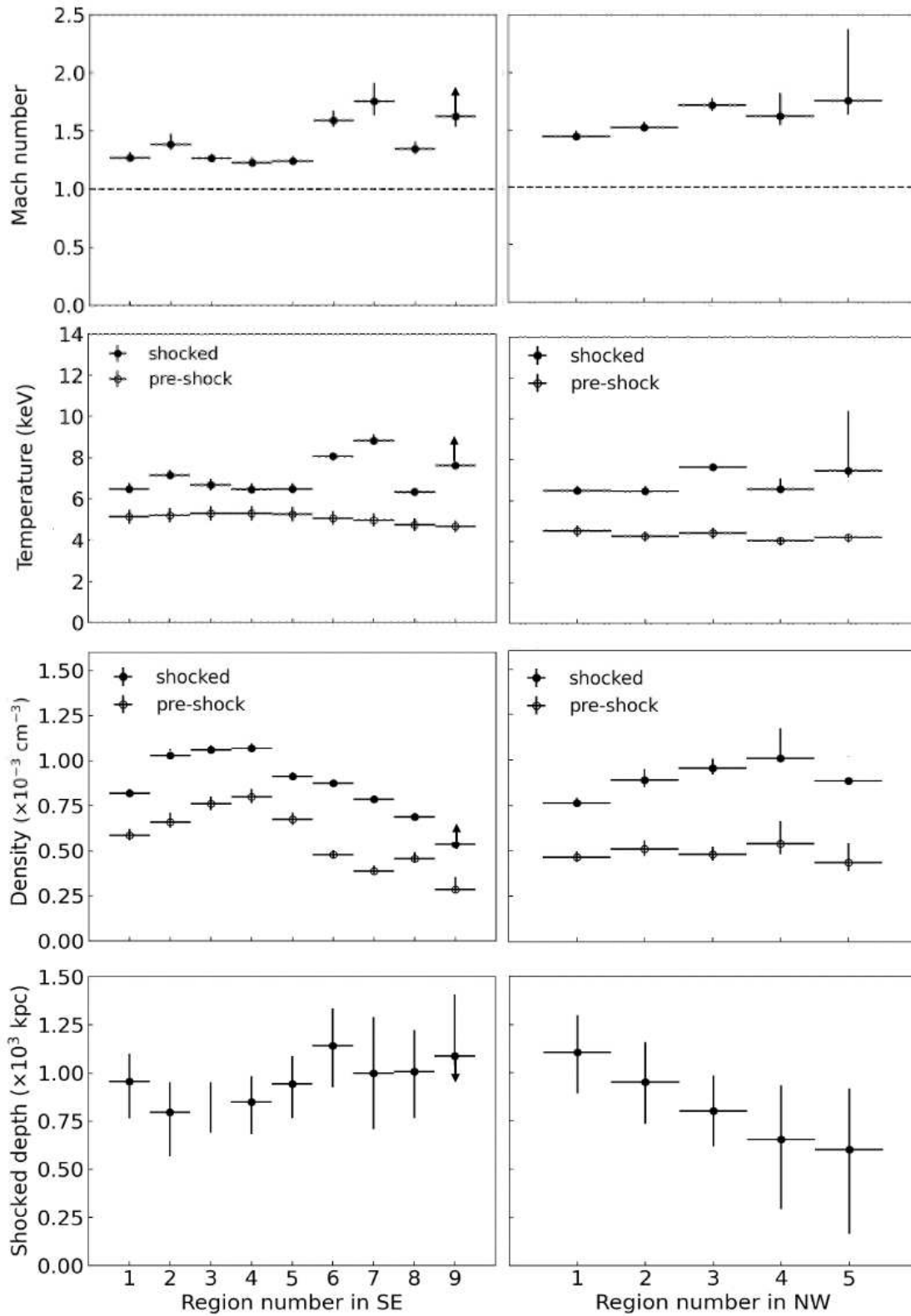


Fig. 10. Results of the 3D merger modeling in the SE (left) and NW (right) shock fronts, respectively. From top to bottom, they represent the Mach number, temperature, density, and depth distributions.

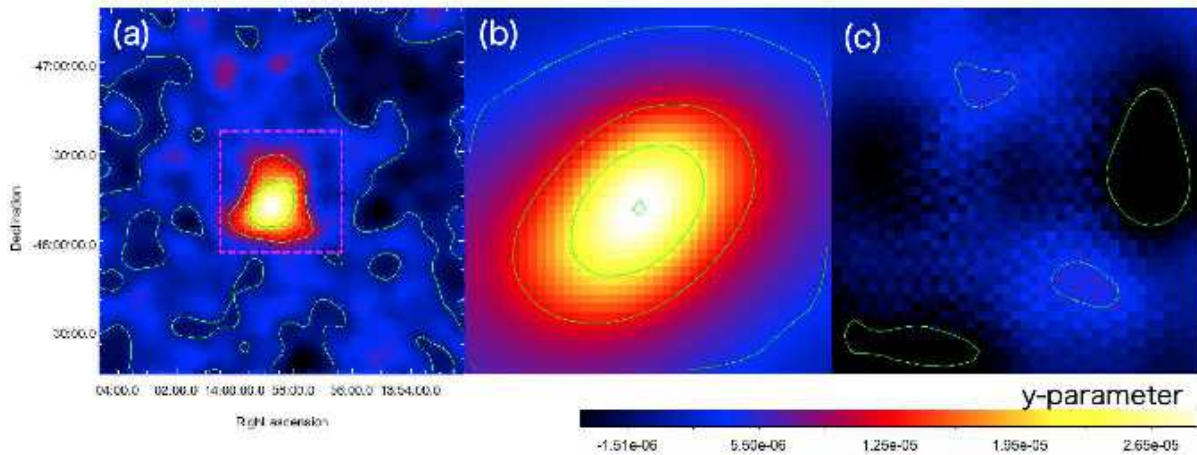


Fig. 11. Left: The ymap of the square region $123' \times 123'$ centered on CIZA J1359 provided by the Planck Release2 NILC ymap (Planck Collaboration et al. 2016). The magenta dotted line indicated the $41' \times 41'$ square region. Center: The ymap based on the X-ray 3D model within the magenta-dotted region. It has an angular resolution of $10'$. Right: Residual map of the center figure subtracting the left figure. The color bar and green contour indicate the y-parameter value, which is dimensionless in units, and the intensity level of 3×10^{-6} .

fluctuations.

These results mean that the 3D merger model with simple assumptions for the shocked condition is consistent with the y-parameter observed by Planck within the CMB fluctuations. However, our analyses here are widely smoothed and the resultant image cannot even resolve the two cluster cores. The current angular resolution of the SZ data does not allow for further investigation of this specific merging cluster.

4 Discussion

4.1 The shock velocity and age inferred from the 3D merger model

In the SE shock, the preshock temperature $kT_{\text{pre}} = 5.3_{-0.3}^{+0.3}$ and the Mach number of ~ 1.3 derived from our model provide the shock front (preshock) velocity of $\sim 1600 \text{ km s}^{-1}$, and the postshock velocity of $\sim 1000 \text{ km s}^{-1}$. We converted these velocities from the shock front frame to the postshock frame, i.e., subtracting the postshock velocity from the velocities of all other regions. Based on the postshock frame, the shock front is moving with a speed of $\sim 1000 \text{ km s}^{-1}$, while the preshock ICM (of the SE cluster) is approaching at $\sim 600 \text{ km s}^{-1}$ (see figure 9.2 in Kato 2018 for a schematic explanation about this calculation process). Similarly, in the NW shock, the shock front is proceeding at a speed of $\sim 900 \text{ km s}^{-1}$, while the preshock ICM (of the NW cluster) is approaching at $\sim 900 \text{ km s}^{-1}$. Combined, the post-shock region is estimated to be expanding at the velocity of $\sim 1900 \text{ km s}^{-1}$ and two clusters are estimated to be merging at the velocity of $\sim 1500 \text{ km s}^{-1}$ on the sky plane. The width of the hot region on the merger axis shown in the upper left panel of figure 3 is $\sim 500 \text{ kpc}$. If the shock waves pass through this width at a constant speed, the age of the shock wave

is estimated to be $\sim 260 \text{ Myr}$.

Based on these velocities and Mach numbers, the kinetic energy flow through the SE shock front can be estimated using the following equation (e.g., Gu et al. 2019; Zhang et al. 2019),

$$F = \frac{1}{2} \rho_{\text{pre}} v^3 \left(1 - \frac{1}{C^2}\right) S,$$

where ρ_{pre} is the preshock ICM mass density², C is a compression number calculated as the ratio of the preshock ICM mass density to the shocked one, and S is the surface area of the shock. From the 3D merger model, the SE shock front has a surface area of $1 \text{ Mpc} \times 1 \text{ Mpc}$ with a Mach number of 1.3 ($C \sim 1.4$) and a velocity of 1600 km s^{-1} , and n_{pre} is $6.0 \times 10^{-4} \text{ cm}^{-3}$. With these parameters, the kinetic energy flow through the shock front is calculated to be $\sim 2.2 \times 10^{45} \text{ erg s}^{-1}$.

Paul et al. (2011) simulated the level of turbulence in a cluster merger and suggested that about 10% of the shock kinetic energy would be converted into turbulence in the post-shock region. If this number is applied to the SE shock of CIZA J1359, the line-of-sight turbulent velocity is calculated to be $\sim 200 \text{ km s}^{-1}$. This value indicates that XRISM *Resolve* observations of CIZA J1359 could potentially be able to distinguish turbulent velocities in the shocked and unshocked regions.

More recently, Kurahara et al. (2022) discovered a candidate for diffuse cluster radio emission in the bridge region using uGMRT and MeerKAT radio observatory data. It is located closely at the NW shock front with a Mach number of 1.7. Meanwhile, they did not find any other diffuse cluster radio emission symptom. If there is a diffuse radio source associated with the higher Mach number shock, it can be relic high-energy electrons reaccelerated by Fermi first-order acceleration. The

² We calculated ρ_{pre} as $7/6 m_{\text{H}} n_{\text{pre}}$, assuming a hydrogen to helium mass ratio of 1:4 and a density ratio of 10:1.

lack of diffuse radio sources in other post-shock regions suggests that the Fermi second-order electron acceleration is inefficient in these young shock regions. A comparison between the data of future XRISM and SKA (Square Kilometre Array) would reveal the nature of turbulence and turbulent acceleration in detail.

4.2 Possibility of local velocity structure in the SE cluster

On the SE shock, Kato (2018) reports a linear brightness enhancement using the Chandra data, which is apparent to the north-east and gradually fades out to the south-west. A similar trend is also visible in our data (see figure 1), and SE 6 and 7 are among the brightest regions in the enhancement. This local linear enhancement was interpreted as a 70 kpc wide “narrow shock”, which has just emerged, in Kato et al. (2015) and Kato (2018).

The 70 kpc narrow shock associated with the southern end of the 500 kpc post-shock region can be consistently understood if there are local fluctuations in the ICM condition, such as local bulk motion. Using the preshock temperature of the SE shock and the derived Mach number at SE 6 and 7, the preshock velocity observed from the postshock region is estimated to be $\sim 1100 \text{ km s}^{-1}$. This is $\sim 500 \text{ km s}^{-1}$ faster than those estimated in other SE regions. In other words, if there is a local bulk velocity of $\sim 500 \text{ km s}^{-1}$ in this region, the enhancement in SE 6 and 7 regions (and also in nearby regions) can be understood.

In the surface brightness ratio plot (the right panel of figure 6), there is a positive residual of 10-20% levels with spiral shape. The residual is also pointed out by Kato (2018) as a surface brightness jump in the Chandra image, which is interpreted as a cold front candidate. If there was a small galaxy group infalling into the southern cluster from the south-east and then curving to the south-west prior to the major merger, residual and local velocity enhancement could take place. Although a more detailed discussion is not possible with the current limited information, a $\sim 500 \text{ km s}^{-1}$ local velocity structure is suggested for a similar spiral residuals by, e.g., Ueda et al. (2019), and in numerical simulations (e.g., Ascasibar & Markevitch 2006). Sanders et al. (2020) also detected signatures of local velocity enhancement of an order of $\sim 500 \text{ km s}^{-1}$ to $\sim 1000 \text{ km s}^{-1}$ in the Perseus and Coma clusters of galaxies. As such, the $\sim 500 \text{ km s}^{-1}$ local velocity structure around SE 6 and 7 is possible.

5 Conclusion

With a 65 ks XMM-Newton EPIC-PN data, we studied the nearby, merging galaxy cluster CIZA J1358.9–4750. The main results of our work are summarized in the following.

- (i) The 2D thermodynamic maps, segmented into ~ 180 regions, indicated the existence of a 7–8 keV high temperature region that extends 500 kpc along the merger axis. The clear increase in temperature, pseudo-pressure and pseudo-entropy at the edges of the hot region led us to conclude that there were two shock waves, one in the SE and the other in the NW.
- (ii) We constructed the 3D original cluster model that reproduces the ICM distribution of the two clusters of galaxies before the collision, using the ICM profile in the outside region. The ratio map of the 3D original cluster model to the observations showed that there is a clear enhancement of temperature and X-ray surface brightness in the hot region while those in the outside region is well reproduced by this simple 3D model.
- (iii) As the Mach numbers obtained by the temperature jump and density jump differ, the 3D merger model was constructed assuming that two temperature components, a shocked component and an unshocked component, overlap in the line of sight. 3D merger model showed that the shocked component with a temperature kT_s of $\sim 8 \text{ keV}$ and a density n_s of $\sim 1.0 \times 10^{-3} \text{ cm}^{-3}$ spreads to a depth of $\sim 1 \text{ Mpc}$ on the shock wave front. We have shown that the SE and NW shock waves are estimated to have Mach numbers of ~ 1.3 and ~ 1.7 , respectively.
- (iv) The y -map based on the 3D merger model agrees with the SZ signals observed by Planck, within the CMB fluctuation level.
- (v) From the 3D merger model, the velocity of the shock wave was estimated to be $\sim 1000 \text{ km s}^{-1}$ for the SE and $\sim 900 \text{ km s}^{-1}$ for the NW, respectively, and the merging velocity was estimated to be $\sim 1500 \text{ km s}^{-1}$. From these velocities, the age of the shock wave is estimated to be $\sim 260 \text{ Myr}$ and the kinetic energy of the SE shock front is estimated to be $\sim 2.2 \times 10^{45} \text{ erg s}^{-1}$. If 10% of this energy is used for a turbulence, the post shock turbulent velocity in the line of sight direction is calculated to be $\sim 200 \text{ km s}^{-1}$.
- (vi) The 3D merger model showed a local enhancement in some regions of the SE shock front (SE 6 and 7). The ratio map of X-ray surface brightness using the 3D original cluster model shows a semi-clockwise spiral enhancement in the SE cluster, suggesting that there may have been local bulk motion in those regions prior to the collision.

Acknowledgments

This work is supported in part by JSPS KAKENHI Grant Numbers 15H03639, 15K17614, 21H01135, 16K05300, and 19K21054.

Appendix. Detail of 3D merger modeling

In this section, we describe the process flow of the 3D merger modeling outlined in section 3.2, using the results in the region SE 3 as an example.

Table 3. Results of two temperatures fitting in the region 3

kT_s (keV)	kT_{us} (keV)	$norm_s^\dagger$ 10^{-5}	$norm_{us}^\dagger$ 10^{-5}	χ^2/dof
$6.7_{-0.6}^{+0.6}$	5.3(fix)	$15.1_{-0.3}^{+0.3}$	0.58(fix)	125/135 = 0.90
$17.7_{-9.4}^{+16.7}$	5.3(fix)	$4.5_{-1.9}^{+6.5}$	$11.6_{-6.6}^{+2.2}$	124/136 = 0.90

† Normalization of the *apec* thermal spectrum, which is given by $\{10^{-14}/[4\pi(1+z)^2 d_A^2]\} \int n_e n_H dV$, where d_A is the angular diameter distance, n_H is the ionized hydrogen density, V is the volume of the region.

According to item 1 in section 3.2, we estimated $norm_{us}$ and kT_{us} at individual l_s , scanning every 1' from 0' to 20' (~ 1600 kpc), as shown in open circle points in the left and middle panels of figure 12. In this figure, the black circle points show the derived $norm_s$ and kT_s by adjusting 2 kT with $norm_{us}$ and kT_{us} fixed at their best-fit values, at individual l_s , according to item 2. At l_s of 10', the results of the 2 kT fitting are shown in figure 13, and the values of each parameter are listed in the upper column of table 3. According to item 3, we derived two Mach numbers for the density and the temperature at each l_s , as shown in the right panel of figure 12. We assumed that in the shocked condition, the temperature is uniformly spread over the emission-weighted temperature and the density has a gradient according to the 3D original cluster model. Errors are evaluated by giving fitting parameters at three levels: maximum, minimum, and best-fit values for the 3D original cluster model, to the parameters of the unshocked regions and those of the preshock condition. We determined the intersection of the density and temperature Mach number curves as the shocked state parameters. However, there are two areas of intersection, one near 80–200 kpc and the other at ~ 1 Mpc. If l_s is 80–200 kpc, the hot region must be thinner along the line of sight than along the merging axis. Since the 3D merger model assumes the major merger on the sky plane, we adopted the intersection near 1 Mpc as our parameter.

Here, can kT_s and l_s be determined by simply fitting the 2 kT models with their parameters free? The lower column of table 3 shows the results of 2 kT fitting with norms free in addition to the parameters of the shocked model. The parameters of the shocked model, especially kT_s , have a large error range. Therefore, we fixed both the kT_{us} and $norm_{us}$, assuming the R-H relations.

We adapted these methods to the shock surface of the south-east (SE 1–9) and northwest (NW 1–5), respectively. As exemplified in table 3, $\chi^2/d.o.f$ value was reasonable in all cases, indicating a good fit. These results are shown in figure 10.

References

- Abbey, T., Carpenter, J., Read, A., et al. 2006, in ESA Special Publication, Vol. 604, The X-ray Universe 2005, ed. A. Wilson, 943
- Akahori, T., & Yoshikawa, K. 2008, PASJ, 60, L19
- . 2010, PASJ, 62, 335
- Akahori, T., Kato, Y., Nakazawa, K., et al. 2018, PASJ, 70, 53
- Akamatsu, H., de Plaa, J., Kaastra, J., et al. 2012a, PASJ, 64, 49
- Akamatsu, H., Takizawa, M., Nakazawa, K., et al. 2012b, PASJ, 64, 67
- Akamatsu, H., Fujita, Y., Akahori, T., et al. 2017, A&A, 606, A1
- Akino, D., Eckert, D., Okabe, N., et al. 2022, PASJ, 74, 175
- Anders, E., & Grevesse, N. 1989, Geochim. Cosmochim. Acta, 53, 197
- Arnaud, K. A. 1996, in Astronomical Society of the Pacific Conference Series, Vol. 101, Astronomical Data Analysis Software and Systems V, ed. G. H. Jacoby & J. Barnes, 17
- Ascasibar, Y., & Markevitch, M. 2006, ApJ, 650, 102
- Bagchi, J., Durret, F., Neto, G. B. L., & Paul, S. 2006, Science, 314, 791
- de Gasperin, F., Rudnick, L., Finoguenov, A., et al. 2022, A&A, 659, A146
- Delabrouille, J., Cardoso, J. F., Le Jeune, M., et al. 2009, A&A, 493, 835
- Diehl, S., & Statler, T. S. 2006, MNRAS, 368, 497
- Ebeling, H., Mullis, C. R., & Tully, R. B. 2002, ApJ, 580, 774
- Fukazawa, Y., Makishima, K., & Ohashi, T. 2004, PASJ, 56, 965
- Ghizzardi, S., Molendi, S., van der Burg, R., et al. 2021, A&A, 652, C3
- Gu, L., Akamatsu, H., Shimwell, T. W., et al. 2019, Nature Astronomy, 3, 838
- Ha, J.-H., Ryu, D., & Kang, H. 2018, ApJ, 857, 26
- Hincks, A. D., Radiconi, F., Romero, C., et al. 2022, MNRAS, 510, 3335
- Ichinohe, Y., Werner, N., Simionescu, A., et al. 2015, MNRAS, 448, 2971
- Johnstone, R. M., Fabian, A. C., Morris, R. G., & Taylor, G. B. 2005, MNRAS, 356, 237
- Kalberla, P. M. W., Burton, W. B., Hartmann, D., et al. 2005, A&A, 440, 775
- Kale, R., Parekh, V., Rahaman, M., et al. 2022, MNRAS, 514, 5969
- Kato, Y. 2018, PhD thesis, University of Tokyo, doi:10.15083/00077893
- Kato, Y., Nakazawa, K., Gu, L., et al. 2015, PASJ, 67, 71
- Kawano, N., Fukazawa, Y., Nishino, S., et al. 2009, PASJ, 61, S377
- Kocevski, D. D., Ebeling, H., Mullis, C. R., & Tully, R. B. 2007, ApJ, 662, 224
- Kuntz, K. D., & Snowden, S. L. 2008, A&A, 478, 575
- Kurahara, K., Akahori, T., Kale, R., et al. 2022, PASJ, submitted
- Lodders, K., Palme, H., & Gail, H. P. 2009, Landolt Börstein, 4B, 712
- Madsen, K. K., Beardmore, A. P., Forster, K., et al. 2017, AJ, 153, 2
- Mann, A. W., & Ebeling, H. 2012, MNRAS, 420, 2120
- Markevitch, M., & Vikhlinin, A. 2007, Phys. Rep., 443, 1
- Miniati, F., Ryu, D., Kang, H., et al. 2000, ApJ, 542, 608
- Nakazawa, K., Sarazin, C. L., Kawaharada, M., et al. 2009, PASJ, 61, 339
- Okabe, N., Akamatsu, H., Kakuwa, J., et al. 2015, PASJ, 67, 114
- Okabe, N., Oguri, M., Akamatsu, H., et al. 2019, PASJ, 71, 79
- Paul, S., Iapichino, L., Miniati, F., Bagchi, J., & Mannheim, K. 2011, ApJ, 726, 17
- Piffaretti, R., Arnaud, M., Pratt, G. W., Pointecouteau, E., & Melin, J. B. 2011, A&A, 534, A109
- Planck Collaboration, Aghanim, N., Arnaud, M., et al. 2016, A&A, 594, A22
- Planelles, S., & Quilis, V. 2009, MNRAS, 399, 410
- Remazeilles, M., Aghanim, N., & Douspis, M. 2013, MNRAS, 430, 370

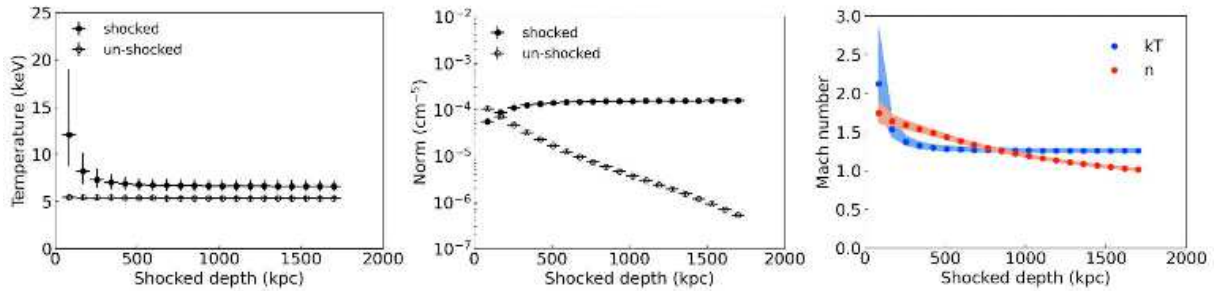


Fig. 12. Temperature (left) and norm (middle) distributions at each l_s obtained by a $2kT$ fitting with the unshocked model fixed in region SE 3. The unshocked component shows values estimated using the 3D cluster model. The Mach number distribution (right) is obtained from the R-H equation for temperature (kT) and density (n), respectively, at each depth using the 3D merger model.

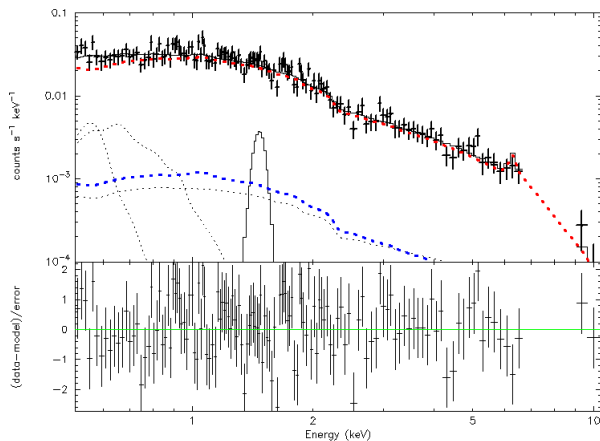


Fig. 13. The result of the spectrum fitting with the $2kT$ model in region SE 3, assuming l_s is $10'$. The red and blue dotted lines indicated shocked and unshocked models, respectively. Their parameters are listed in the upper column of table 3

Science, 330, 347

Vikhlinin, A., Kravtsov, A., Forman, W., et al. 2006, *ApJ*, 640, 691

Vikhlinin, A., Markevitch, M., Murray, S. S., et al. 2005, *ApJ*, 628, 655

Šuhada, R., Song, J., Böhringer, H., et al. 2012, *A&A*, 537, A39

Zhang, C., Churazov, E., Forman, W. R., & Lyskova, N. 2019, *MNRAS*, 488, 5259

Ricker, P. 2004, 35, 3617

Ricker, P. M., & Sarazin, C. L. 2001, *ApJ*, 561, 621

Russell, H. R., Sanders, J. S., & Fabian, A. C. 2008, *MNRAS*, 390, 1207

Ryu, D., Kang, H., Hallman, E., & Jones, T. W. 2003, *ApJ*, 593, 599

Sanders, J. S., Dennerl, K., Russell, H. R., et al. 2020, *A&A*, 633, A42

Sanderson, A. J. R., O'Sullivan, E., Ponman, T. J., et al. 2013, *MNRAS*, 429, 3288

Sarazin, C. L., Finoguenov, A., Nakazawa, K., Wik, D. R., & Clarke, T. E. 2010, in *AAS/High Energy Astrophysics Division*, Vol. 11, AAS/High Energy Astrophysics Division #11, 34.24

Sarazin, C. L., Finoguenov, A., Wik, D. R., & Clarke, T. E. 2016, *arXiv e-prints*, arXiv:1606.07433

Skillman, S. W., O'Shea, B. W., Hallman, E. J., Burns, J. O., & Norman, M. L. 2008, *ApJ*, 689, 1063

Snowden, S. L., Mushotzky, R. F., Kuntz, K. D., & Davis, D. S. 2008, *A&A*, 478, 615

Sun, M., Voit, G. M., Donahue, M., et al. 2009, *ApJ*, 693, 1142

Takizawa, M. 2008, *ApJ*, 687, 951

Ueda, S., Ichinohe, Y., Kitayama, T., & Umetsu, K. 2019, *ApJ*, 871, 207

van Weeren, R. J., Intema, H. T., Röttgering, H. J. A., Brüggén, M., & Hoeft, M. 2011, *Mem. Soc. Astron. Italiana*, 82, 569

van Weeren, R. J., Röttgering, H. J. A., Brüggén, M., & Hoeft, M. 2010,